
NONLINEAR INFERENCE CAPACITY OF FIBER-OPTICAL EXTREME LEARNING MACHINES

A PREPRINT

Sobhi Saeed¹, Mehmet Müftüoğlu¹, Glitta R. Cheeran¹, Thomas Bocklitz^{1,2}, Bennet Fischer¹, and Mario Chemnitz^{1,3,*}

¹Leibniz-Institute of Photonic Technology, Albert-Einstein-Str. 9, 07745 Jena, Germany

²Institute of Physical Chemistry, Friedrich Schiller University Jena, Helmholtzweg 4, 07743 Jena, Germany

³Institute of Applied Optics and Biophysics, Friedrich Schiller University Jena, Albert-Einstein-Str. 15, 07745 Jena, Germany

*mario.chemnitz@leibniz-ipht.de

February 3, 2025

ABSTRACT

The intrinsic complexity of nonlinear optical phenomena offers a fundamentally new resource to analog brain-inspired computing, with the potential to address the pressing energy requirements of artificial intelligence. We introduce and investigate the concept of nonlinear inference capacity in optical neuromorphic computing in highly nonlinear fiber-based optical Extreme Learning Machines. We demonstrate that this capacity scales with nonlinearity to the point where it surpasses the performance of a deep neural network model with five hidden layers on a scalable nonlinear classification benchmark. By comparing normal and anomalous dispersion fibers under various operating conditions and against digital classifiers, we observe a direct correlation between the system's nonlinear dynamics and its classification performance. Our findings suggest that image recognition tasks, such as MNIST, are incomplete in showcasing deep computing capabilities in analog hardware. Our approach provides a framework for evaluating and comparing computational capabilities, particularly their ability to emulate deep networks, across different physical and digital platforms, paving the way for a more generalized set of benchmarks for unconventional, physics-inspired computing architectures.

Keywords: Optical Neural Networks, Extreme Learning Machine, Supercontinuum Generation, Nonlinear Fiber Optics, Optical Soliton, Machine Learning

1 Introduction

The rapid advancement of artificial intelligence has sparked renewed interest in brain-inspired hardware, particularly optical implementations that promise energy-efficient solutions for AI acceleration and intelligent edge sensing. Traditional computing architectures face significant challenges when executing analog neural networks, resulting in substantial energy, water, and computational time requirements for operating large networks on conventional digital processors (i.e., CPUs, GPUs, TPUs).

Optical approaches have garnered particular attention due to their intrinsic parallelism and scalability across multiple optical degrees of freedom, offering reduced energy consumption [1]. Unlike electronic solutions, a primary challenge in realizing competitive neuromorphic optical hardware lies in the all-optical implementation of nonlinearity to circumvent the electro-optical bottleneck toward deep all-optical architectures [2], [3].

Nonlinearity is crucial for emulating synaptic switching behavior in information networks and enabling advanced learning capabilities, including improved accuracy and generalization. In deep networks, this issue is often addressed through multiple layers, which offer higher nonlinear mapping capabilities of the model. The concept of "nonlinear mapping capability" refers to a system's ability to transform input data into higher-dimensional spaces where previously inseparable patterns become linearly separable. Moving to hardware, physical substrates can inherently provide complex nonlinear responses through their natural dynamics without the need for additional layers or computational resources. In optics, taking advantage of the nonlinearity offered by light-matter interactions in the media, while actively studied [4], is widely assumed to be complicated and inefficient due to its high-power demands [5].

Several recent studies suggest alternatives to realize non-trivial nonlinearity in optical systems. These include electronic feedback loops to electro-optic modulators [6], [7], saturable absorption [8] complex active gain dynamics in mode-competitive cavities [9], and, most recently, repeated linear encoding through multiple scattering of input data [10], [11].

Neuromorphic computing with wave dynamics offers a promising approach to the elegant utilization of natural nonlinear dynamics in physical substrates. In optics, the concept aligns with Extreme Learning Machines (ELM) - a form of reservoir computing [12], [13] without internal recurrence. Unlike other optical implementations, the learning machine comprises multiple virtual nodes that are coupled by the intrinsic feed-forward propagation dynamics of a single optical component, such as a fiber. This concept, recently proposed by Marcucci et al. [14], utilizes process-intrinsic, nonlinear mode interactions from natural waveguide dynamics as a computing resource. Experimental demonstrations include nonlinearly coupling spatial modes in multimode fibers [15] and spectral frequency generation in single-mode fibers [16], [17], [18]. However, analog wave computers have a common diffi-

culty: the systems are generally complex and cannot be easily mapped to practical computing models, a critical challenge lies in the diversity of existing approaches and the general inability to measure a system's nonlinear mapping capabilities independent of specific tasks and to correlate them with learning abilities. This transformation is fundamental to solving complex tasks. Current approaches in the optical community empirically test new nonlinear systems on this capability through task-specific image recognition benchmarks. Here, it is common practice to compare, e.g., accuracies across system configurations to demonstrate improvements and to relate those improvements to the scaling in the learning behavior of deeper, hence more nonlinear neural networks computer models.

In particular, the MNIST dataset is frequently used as a benchmark. However, it is not highly nonlinear, as a logistic regression can achieve approximately 92% accuracy [19]. Similarly, linear Support Vector Machines (SVMs), which leverage kernel tricks to project input data into higher-dimensional spaces for linear separation, demonstrate comparable performance. Furthermore, performance improvements in big networks cannot be clearly attributed to stronger synaptic activation (i.e., deepness) yet might also result from increased connectivity as we will discuss further down in this paper. Task-specific benchmarks thus prove unsuitable for demonstrating deeper network activity. The question of nonlinearity's relevance in neural networks also remains largely unexplored in computer science, with only limited investigations into non-binary nonlinear activation functions, such as a multi-step perceptron [20] or trainable spline activation functions [21].

This work attempts to better understand and quantify the nonlinear inference capacity using a scalable, task-independent dataset and validate it using two different optical fiber processors. This investigation is particularly relevant for comparing computational capabilities across different physical substrates.

We begin with illustrating the operation principle of a frequency-based ELM in a single optical fiber, as an arbitrary kernel machine, we refer to it from this chapter onward as fiber-optical ELM. We then assess the inference capabilities of two different nonlinear systems distinguished by their dispersion properties and corresponding nonlinear dynamics (i.e., self-phase modulation and soliton fission).

We assess the nonlinear inference capacity of the two different fiber-optical machines using a scalable spiral dataset, where increasing the angular span progressively challenges separability. These comparisons were conducted under different system configurations, including variations in fiber types, different numbers of system read-outs, and different power levels. Observations on both datasets are compared to digital classifier models, like neural networks and support vector machines, providing a strong basis for drawing parallels between the depth of digital networks and the nonlinear inference capacity of our analog computing systems.

2 Materials and methods

2.1 Experimental setup

We conducted experiments using a fiber-optical extreme learning machine in the frequency domain. The experimental system (see Fig. 1d) comprises a femtosecond laser source (Toptica DFC) operating at 80 MHz repetition rate with 70 nm bandwidth centered at 1560 nm, followed by an erbium-doped fiber amplifier (Thorlabs EDFA300p) operated at 25% pump current to compensate for system losses. Data is encoded using a polarization-maintaining programmable spectral filter (Coherent Waveshaper 1000A/X) operating in the extended C- to L-band (1528-1602nm), which allows to independently modify spectral phase and amplitude across 400

frequency channels for both dispersion compensation and phase information imprinting. The initially chirped pulses are pre-compressed through a dispersion-compensating fiber (Thorlabs PMDCF, 1m length) to 400 fs before entering the spectral filter. A particle swarm optimization algorithm in conjunction with optical autocorrelation measurements has been utilized to further optimize the input pulse phase to obtain 135 fs [22], [23] before entering the main processing unit - a highly nonlinear fiber. Two nonlinear fibers were in use: (1) Thorlabs HN1550, 5m length with all-normal dispersion (-1 ps/nm/km @1550nm), and 10.8 $W^{-1}km^{-1}$ nonlinear coefficient, and (2) Thorlabs PMHN1, 5m length, with anomalous dispersion ($+1$ ps/nm/km @1550nm), and 10.7 $W^{-1}km^{-1}$ nonlinear coefficient. The output is measured using an optical spectral ana-

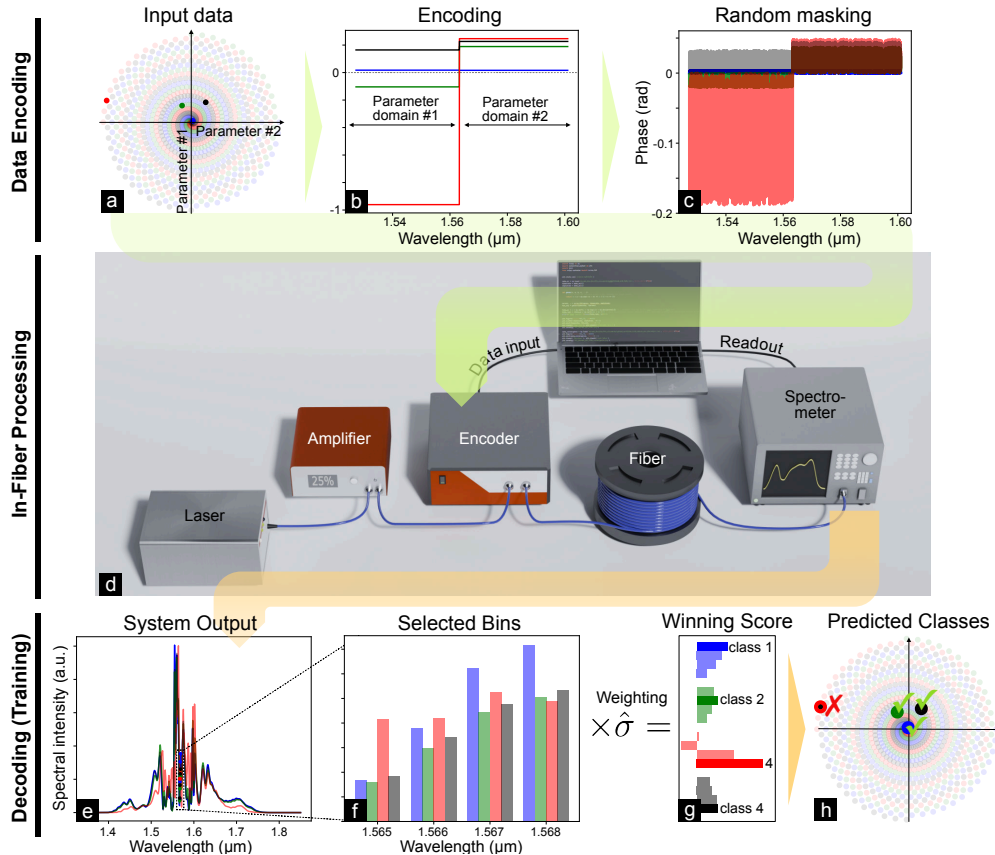


Figure 1: Illustration of the data flow in the fiber-based neuromorphic system using an example from the spiral dataset. (a) Input data: four sample points were selected from four different spirals. (b) Corresponding data encoding: the first half of the spectral encoding range (limited by the WaveShaper) encodes the X_1 -coordinate of a data tuple; the second half encodes the X_2 -coordinate. (c) Encoding phase after multiplying with a constant phase scale factor and an arbitrary but fixed mask. (d) The experimental setup used for processing. A computer is used as I/O device and is not part of a feedback loop. (e) Linear spectral intensities at fiber output corresponding to the four sample inputs. (f) Linear spectral intensities at the selected, optimized search bins serving as system read-outs. (g) Prediction scores obtained by multiplying the read-outs with the trained weight matrix. Per sample, scores are sorted from class 1 to 4, from top to bottom. The highest values in a vector of four (i.e., $\text{argmax}(\mathbf{Y}^{\text{score}})$) determines the predicted class. (h) Prediction results: points represent the predictions, while circles around these points indicate the true class labels, the examples contain one misclassification indicated by the red cross.

lyzer (Yokogawa AQ6375E) and analyzed on a standard office computer. All components are fiber-coupled and polarization-maintaining, ensuring stable operation in a compact footprint.

We illustrate how the fiber-optical ELM processes information with the example of a four-arm spiral dataset. For the spiral classification benchmark, the inputs consist solely of two coordinates for each data point, with each coordinate tuple assigned to one point of the four spirals.

Further details about the dataset are provided in the results section. The coordinate tuples are encoded into the spectral phase of a femtosecond pulse using a phase mask, where the first half of the phase mask corresponds to the X_1 -coordinate and the second half corresponds to the X_2 -coordinate, as illustrated in Fig. 1b. To enhance the system’s sensitivity to the encoded inputs, the phase mask is multiplied by a random mask, shown in Fig. 1c. This approach is common for optical reservoir computers [24], [25], [26], [27], as it leverages the system’s sensitivity to phase jumps rather than absolute phase, ensuring a maximized system response. As a result, the output signals corresponding to different encodings become more distinguishable.

2.2 Supervised offline training

Following the principles of extreme learning machines [20], we train only the output layer. This method leverages the fiber-optical ELM’s inherent ability to perform complex, high-dimensional transformations efficiently, reducing the computational burden associated with traditional training. Hence, to translate the output spectra of the system into an interpretable inference, we train a weight matrix based on selecting a subset from all wavelength recordings. From this chapter onward, we call the locations of the wavelength windows “search bins” and their corresponding intensities “read-outs”.

We select a user-defined number of search bins n using an optimization algorithm called *Equal Search*, a straightforward method that identifies combinations of equally spaced search bins, as described in [17]. From the resulting combinations, we choose the one that minimizes the mean square error ($MSE = \frac{1}{N} * \sum (\mathbf{W}\mathbf{X} - \mathbf{Y})^2$, N is the number of test data while applying cross validations) over five cross-validations. The weight matrix \mathbf{W} ($R^m \times R^n$ with m output classes and n search bins) is calculated using solely linear regression, as given by the Moore-Penrose inverse

$$\mathbf{W} = (\mathbf{X}^T \mathbf{X})^{-1} \mathbf{X}^T \mathbf{Y} \quad (1)$$

where \mathbf{X} is the read-outs vectors (intensities at selected search bins of dimension $R^n \times R^k$ with k samples), and \mathbf{Y} is the task’s label vectors (ground truth of dimension $R^m \times R^k$). We experimented with incorporating the ridge term while training the system; however, we found it consistently yielded worse results (e.g., see long-term measurements in Fig. 2A in appendix).

After training the weight matrix, classification is performed by acquiring the output values at the best combination of search bins identified before. These values

are stored in a vector and multiplied by the weight matrix, producing another vector, referred to as the prediction score $\mathbf{Y}^{score} = \mathbf{W}\mathbf{X}$. A winner-takes-all decision, i.e. $\mathbf{Y}^{class} = \arg \max(\mathbf{Y}^{score})$ is then performed on the Prediction Score vector, classifying the test data based on the index of the highest score, as shown in Figs. 1g-h. We compare systems based on task-specific classification accuracy in percent (%), which is defined by the ratio of number of correct class predictions over the total number of samples.

Fig. 2 illustrates the nonlinear projection capabilities of our fiber-optical neural network through measured spectral response to input data tuples (X_1, X_2) sampled from four distinct classes in a two-dimensional coordinate system. The *Equal Search* algorithm identified four optimal search bins (Figs. 2a->d) demonstrating highly distinct separation between the data classes in the spectral domain. Particularly noteworthy are the projections shown in Figs. 2b-c, where the nonlinear fiber transformation achieves nearly ideal plane-wise separation of the classes in three dimensions, providing clear evidence of the system’s powerful separation capabilities. In contrast, Figs. 2e-f present randomly selected wavelength windows where the class separation is poor or non-existent, with data points from different classes showing significant overlap. This behavior effectively showcases the fundamental principle proposed by Huang et al. in their original ELM framework: ELMs can be understood as arbitrary kernel machines that, in optimal cases, provide hidden nodes with kernel response functions capable of transforming complex problems into linearly separable ones [20]. Following this interpretation, the performance of an ELM improves with access to a greater variety of kernel functions - a key insight that leads to our hypothesis that physical systems exhibiting richer nonlinear dynamics should outperform those with weaker nonlinearity in classification tasks.

3 Results and discussion

In this section, we demonstrate the capability of a fiber-optical ELM to effectively handle highly nonlinear tasks, exemplified by the spiral classification benchmark. The spiral classification task has emerged as a critical benchmark in the machine learning community [28] for evaluating neural networks’ capability to handle tangled data points and to learn nonlinear decision boundaries. This two-dimensional dataset, featuring interleaved spiral arms over an angular span of 2π , is intrinsically not linearly separable and poses a particular challenge for optical computing systems due to the inherent difficulty in implementing nonlinear activation functions in the optical domain. However, recent breakthroughs have demonstrated significant progress in this area, with recent notable achievements including on-chip complex-valued neural networks reaching 95% accuracy on a 2-arm spiral classification [29] and a three-layer optoelectronic neural network achieving 86% accuracy on a 4-arm spiral classification [30].

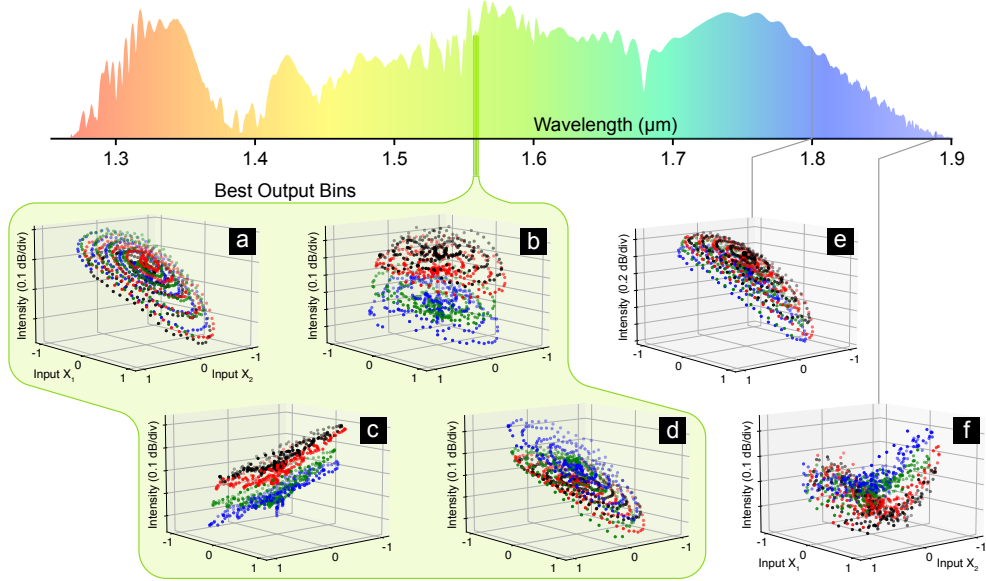


Figure 2: 3D plots illustrating the relationship between output spectral intensity of a supercontinuum from an anomalous dispersive fiber and the input coordinates for all given samples. (a-d) Logarithmic spectral intensity versus input coordinates (X_1 , X_2) at the optimized, selected search bins, demonstrating the system’s intrinsically distinguishable response to different classes. (e-f) Spectral intensity versus input coordinates at two randomly selected wavelength windows. Both examples are still >10 dB above the spectrometer’s noise floor.

Building upon these advances, we introduce an enhanced version of this benchmark that increases the hardness of the task. We generalized the spiral dataset by a free parameter, called the maximum angular span θ_{max} , which controls the complexity of the spiral benchmark, making it particularly effective for illustrating the impact of the network depth and the system’s nonlinear dynamics on the inference capabilities of digital and optical neuromorphic systems, respectively. As later shown in Figs. 5a, 6. As such, it is an excellent general measure of the nonlinear inference capacity of new neuromorphic physical substrates. The data points are generated using analytic equations (Eq. 2), allowing flexibility in defining the number of phase-shifted spiral arms (number of classes, controlled by index k) and their wraps around the center (controls the complexity of the task). The number of wraps defined by a full 360° turn around the center is controlled by θ_{max} , where the number of wraps equals $\theta_{max}/2\pi$. For the presented results, we generated 250 points per spiral, yielding 1000 total points across four spirals. From this set we use 800 randomly selected points (200 per spiral) to train the system and kept 200 points (50 points per spiral) for testing after training (4:1 data split ratio).

$$\begin{aligned} X_1 &= \frac{\theta}{\theta_{max}} \cos\left(\theta + k\frac{\pi}{2}\right) & \theta \in [0, \theta_{max}] \\ X_2 &= \frac{\theta}{\theta_{max}} \sin\left(\theta + k\frac{\pi}{2}\right) & k \in \{0, 1, 2, 3\} \end{aligned} \quad (2)$$

We evaluated our fiber-optical ELM on the spirals benchmark, with its increasing nonlinearity as θ_{max} increases (e.g. from 0.5π to 10π), which is an ideal task to demon-

strate the fiber-optical ELM’s ability to handle highly nonlinear problems. Fig. 3 illustrates the classification results for $\theta_{max} = 10\pi$, corresponding to 5 wraps around the center per spiral. Figs. 3a-b show the average and the standard deviation (STD) of the spectral intensities for both fiber types, normal dispersion (ND) fiber and anomalous dispersion (AD) fiber, respectively, measured under the same excitation conditions (i.e., 18.45 mW, 136 fs, cp. Tab. 1). The difference in standard deviations between the two cases arises from using different scale factors in the encoding phase for the two fibers.

We chose the scale factors according to the highest classification accuracy obtained during our experiments with various scale factors (see Fig. 4A in Appendix). Specifically, we use $\pi/2$ for the ND fiber and $\pi/16$ for the AD fiber, resulting in a larger STD for the ND case. Our Equal Search analysis allows us to compare the system’s performance for various numbers of search bins. In Fig. 3c, we observe increasing the number of search bins increases system accuracy for both fibers. The AD fiber achieves superior performance on the spiral benchmark ($>95\%$ accuracy for 35 bins and up) compared to ND fiber, which reaches the best accuracy of 91.5% with 50 bins before going into overfitting (i.e., test accuracy diverges from training accuracy).

We test the system’s performance on a low nonlinear task known to be solvable to a high degree by simply using linear classifiers. We identified this dataset to be suitable for this purpose. The MNIST dataset is a widely used collection of handwritten digits from 0 to 9 (i.e., 10 classes), stored as 28×28 pixels gray-valued images, that serves

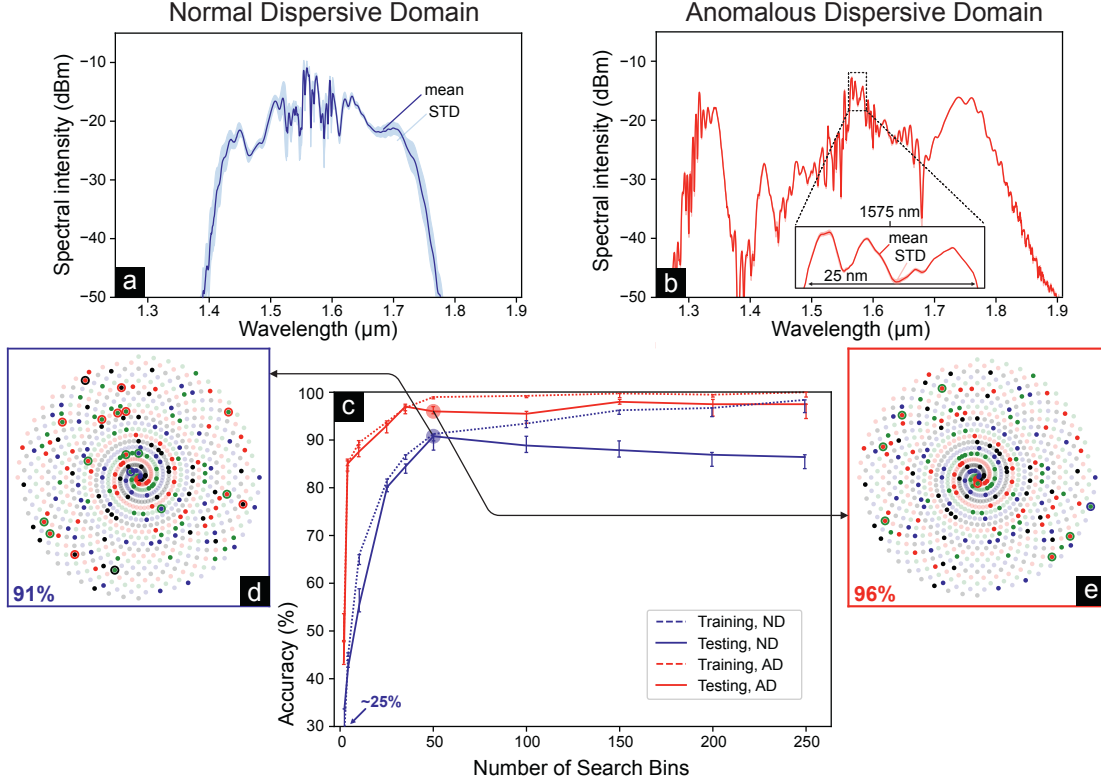


Figure 3: (a) Average and standard deviation (STD) of output spectral intensities for the spirals dataset in the normal dispersion (ND) case. (b) Average and std of output spectral intensities for the spirals dataset in the anomalous dispersion (AD) case. (c) Classification accuracy achieved for both fiber types as a function of the number of search bins. (d) Classification results for the ND case using 50 search bins. (e) Classification results for the AD case using 50 search bins.

as a standard benchmark in machine learning. The dataset used in this study is sourced from the TensorFlow library (tensorflow_datasets).

We trained the system on the first 2100 images and tested it on 300 images previously unseen by the system using both normal and anomalous dispersion fibers. To encode the MNIST images, we first crop an 18×18 -pixel window to meet the data input limitations of the Waveshaper. The cropped images were then flattened row-wise from top to bottom into 1D signals corresponding to pixel intensities. These 1D signals were multiplied by a random mask and a phase scale factor before adding them to an optimized phase profile, yielding the encoding phase (cp. Fig. 3Ad) which modifies the optical signal using the Waveshaper, hence encoding the input information, before propagating through the fiber. At the output layer, the system follows the same procedure as in the spiral benchmark. It stores the output read-outs at the newly selected search bins and translates these read-outs into an interpretable prediction score by multiplying the read-outs vector with a trained weight matrix. The highest value in the prediction score (i.e., $\text{argmax}(\mathbf{Y}^{\text{score}})$) determines the predicted class. Fig. 3A in Appendix illustrates all input and output levels for an MNIST test image.

Unlike the spiral benchmark, the system demonstrates similar performance on MNIST when using ND fiber (89.33% accuracy) and AD fiber (87.3% accuracy), as shown in Figs. 4d-e, respectively. Both cases surpass the baseline of 83.7% for linear regression on the data [31] and perform similarly to a support vector machine (SVM) with a linear kernel which achieves about 91% in accuracy with only 20 support vectors (cp. Figure 1A in Appendix). Classification accuracy further improves with an increased number of search bins, as illustrated in Fig. 4c.

We hypothesize that the higher nonlinear mapping introduced by the AD fiber does not significantly affect system performance for a task with low nonlinearity, such as MNIST. The slightly better performance observed with the ND fiber in our setup can be attributed to a more extensive optimization process during the selection of the optimal encoding phase scale factor. Specifically, when using the ND fiber, we conducted multiple experiments with different phase scale factors and selected the one that achieved the highest accuracy. For both fibers, a phase scale factor of $\frac{\pi}{4}$ was ultimately chosen. Figs. 4a-b depict the average spectral output intensities and their corresponding standard deviations for both ND and AD fibers. The STD values in the two cases are comparable because we used the same

phase scale factor.

The confusion matrices and per-class accuracy for both cases are presented in Figs. 4d-e. A notable observation is the misclassification between the digit classes 3 and 5 and classes 4 and 9, which likely arises from their similar 1D intensity profiles.

To assess robustness, we conducted a long-term evaluation involving training the system on 3000 images and testing it on 35000 images over an acquisition period of 35 hours. The system maintained an accuracy of 84.69%, with only a modest 4.5% drop over the extended testing period, underscoring its reliability and resilience. Further details of this robustness analysis are provided in Fig. 2A in the appendix.

We further investigate the impact of input power (consequently the system’s nonlinear mapping capability) on the performance of our fiber-optical ELM handling increasingly harder task, by changing the attenuation applied on the input signals (0, 2, 4, 6, 8 dB), while progressively increasing the spirals’ θ_{max} ($0.5\pi, 2\pi, 4\pi, 8\pi, 10\pi$), thereby increasing the complexity of the classification task. Additionally, we benchmark our system against digital neural networks with different configurations for both the spiral and MNIST datasets. We based our comparison between the optical and digital systems solely on the achieved results as we fed both systems with the exact same dataset with a fixed training-testing split ratio.

The results highlight the fiber-optical ELM’s efficiency in handling highly nonlinear tasks, such as the spiral bench-

mark with a large angular span (θ_{max}), outperforming a 5-hidden-layer digital neural network with 1024 nodes for $\theta_{max} > 10\pi$. Furthermore, the results demonstrate the critical role of network depth to address highly nonlinear tasks in digital neural networks. As shown in Fig. 5a, deeper networks offer significant performance advantages when handling tasks with high nonlinearity, despite having the same number of nodes as their shallower counterparts. Distribution of the nodes is illustrated in Tab. 1A in Appendix. Fig. 5b illustrates the accuracy achieved using the ND fiber on the spiral benchmark with different maximum angular spans ($\theta_{max} = 0.5\pi, 2\pi, 4\pi, 8\pi, 10\pi$), under different attenuation levels (0, 2, 4, 6, 8 dB), represented as heatmap rows and columns, respectively. Fig. 5c presents the corresponding results for the AD fiber. Both cases use 50 search bins. We notice that applying attenuation (decreasing the input power) has a more pronounced effect on system performance for highly nonlinear tasks (e.g., spirals with high θ_{max}) compared to its impact on low nonlinear tasks (spirals with low θ_{max} and MNIST, cp. Fig. 6). This performance degradation stems from the reduced nonlinear mapping capability of the system at lower input power levels. However, increasing the number of search bins mitigates the loss in nonlinear mapping induced by attenuation (cp. Fig. 6a), this is in accordance with previous observations on comparable problems [17]. Interestingly, the AD fiber shows particularly better performance at lower input power levels for more complex tasks compared the ND fiber, though with greater fluctuations.

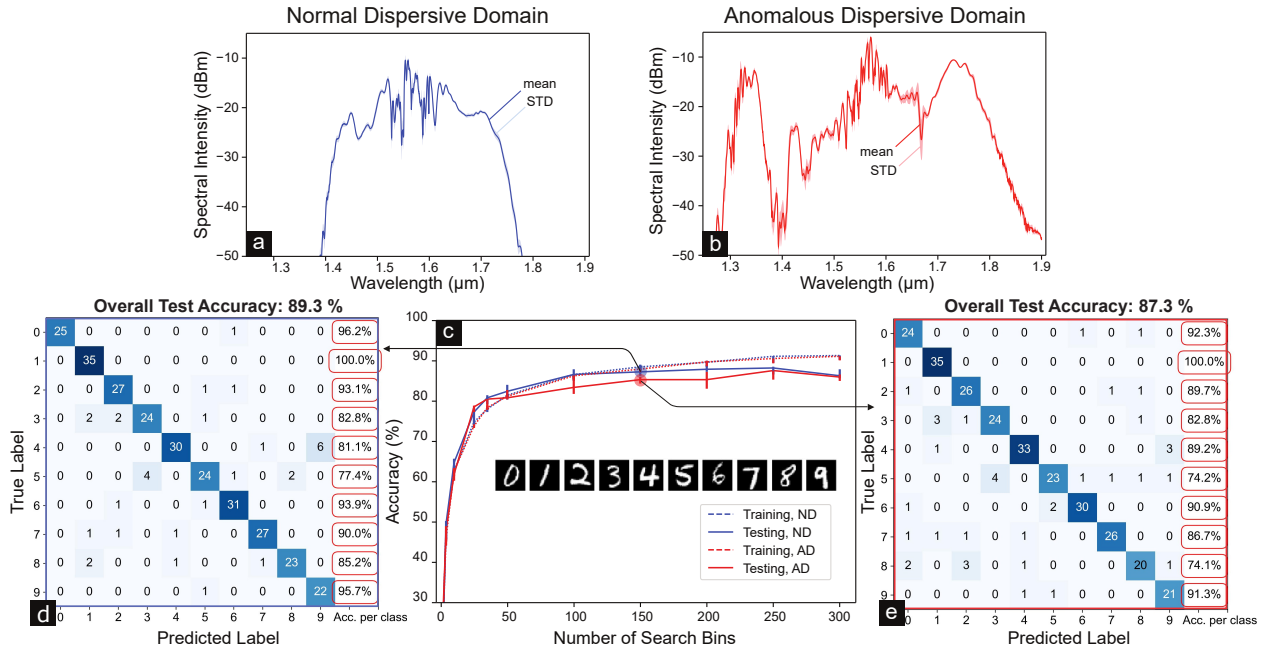


Figure 4: (a, b) Average and standard deviation (STD) of measured output spectral intensities for the MNIST dataset in the (a) normal dispersion (ND) case and (b) anomalous dispersion (AD) case. (c) Classification accuracy achieved across 300 MNIST test samples as a function of the number of search bins for both fiber types. (d, e) Confusion matrices of our systems for unseen test data for the (d) ND case (achieved accuracy 89.33%), and (e) AD case (achieved accuracy 87.3%) using 150 search bins for both cases.

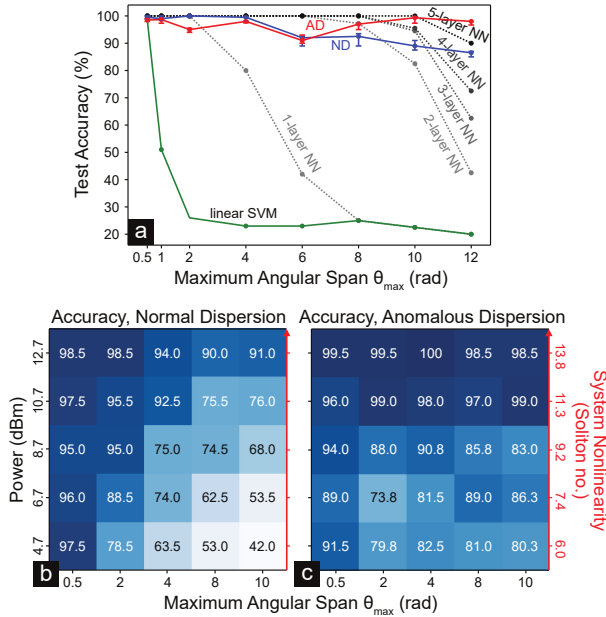


Figure 5: (a) Best test accuracy on 200 spiral data samples achieved by digital classifiers (a linear kernel support vector machine with 100 support vectors, and neural networks in different configurations (cp. Tab. 1A); all trained for 1000 training epochs) and our fiber-optical ELM using 100 search bins for increasing nonlinear problem hardness in the spiral task, defined by the maximum angular span θ_{max} . (b,c) Test accuracies on 200 spiral data samples as a function of system nonlinearity (or attenuation) and maximum angular span for both, (b) normal dispersion and (c) anomalous dispersion.

These fluctuations are most evident in the unexpectedly high accuracy for $\theta_{max} = 8\pi$ at attenuation of 6 dB (input power = 6.7 dBm). In all subfigures of Fig. 5, the system nonlinearity is defined by the soliton number:

$$N = \sqrt{\frac{\gamma P_0 T_0^2}{|\beta_2|}} \quad (3)$$

$$P_0 = \frac{P_{avg}}{T_0 \cdot f_{rep}} \quad (4)$$

γ is the nonlinear coefficient ($W^{-1}km^{-1}$), P_0 is the peak power, T_0 is the measured pulse width (seconds) and β_2 is the dispersion coefficient (s^2/m), and f_{rep} is the laser repetition rate in (Hz). Tab. 1 shows the power and autocorrelation measurements for the presented results.

The soliton number corresponds to a normalized nonlinear gain parameter of a waveguide system which is proportional with peak power P_0 and, hence, inversely to the attenuation level. We emphasize parametrizing the system’s nonlinear mapping capability using the soliton number rather than input power alone, as it reflects both the peak power and the pulse width of the input signal,

Table 1: Pulse width and peak power at the input of the highly nonlinear fiber (HNLf) for various encoding conditions (attenuation), calculated using average power and pulse width (both are measured before propagating through the fiber). The pulse width was measured using an APE autocorrelator (pulseCheck NX 50). The average of 16 scans over a range of 5 ps was fitted to a Lorentzian function to determine the pulse width.

Encoding attenuation applied (dB)	Average power measured (mW)	Pulse width measured (fs)	Peak power calculated (W)
0	18.56	136	1705.88
2	11.66	146	998.29
4	7.41	155	597.58
6	4.72	157.5	374.60
8	3.04	161	236.02

hence the signal’s coherence, which is essential for super-continuum generation [32].

Lastly, we demonstrate that increasing the optical system’s nonlinearity (indicated by the soliton number) has a similar impact on the achieved results in an optical neuromorphic system, to increasing the depth of a digital neural network. Particularly, investigating these performance trends similarities on a highly nonlinear task represented by the spiral benchmark with an angular span of $\theta_{max} = 10\pi$ and a low nonlinear task represented by MNIST.

Fig. 6a presents the test accuracy achieved for MNIST and the spiral benchmark (with $\theta_{max} = 10\pi$) at various attenuation levels. The results are shown for two configurations: using 150 search bins (solid lines) and 50 search bins (dotted lines), while coupling with an ND fiber and maintaining the same system configuration described earlier.

We observe that increasing the system’s nonlinearity does not enhance its performance on the MNIST dataset. In contrast, higher nonlinearity significantly improves performance on the spiral benchmark with a high angular span ($\theta_{max} = 10\pi$). A similar trend is evident when solving these benchmarks using digital neural networks. Fig. 6b illustrates the achieved test accuracy for different configurations of a multilayer neural network, yet they all have the same total number of nodes, 400.

MNIST is solvable with 10 nodes as shown in Fig. 1A in Appendix. However, we needed a bigger network to solve the spiral Benchmark. The 400 nodes are distributed across the hidden layers as shown in Tab. 2A. Number of hidden layers is indicated by the x axis in Fig. 6b. From Fig. 6b, as expected, increasing the depth of the network has a negligible impact on the test accuracy achieved for the MNIST dataset, they only demonstrate faster convergence, enabling the model to stabilize with fewer training epochs. In contrast, deeper networks provide a significant advantage when handling highly nonlinear tasks, such as the spiral benchmark with $\theta_{max} = 10\pi$. Specifically, 4- and 5-hidden-layer networks with 400 nodes (see Fig. 6b) out-

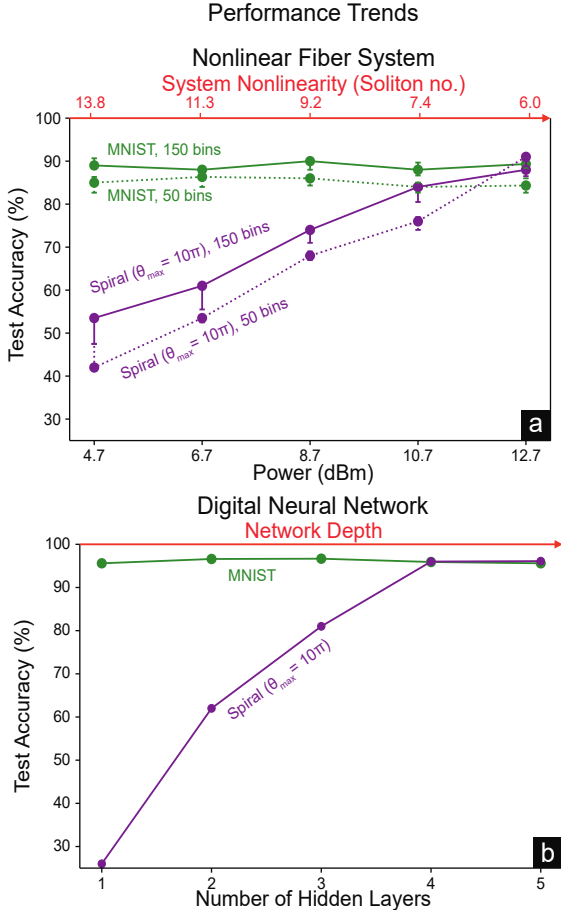


Figure 6: (a) Performance trends of the fiber-optical ELM on a highly nonlinear task (spiral benchmark) and a low nonlinear task (MNIST) under varying attenuation levels. (b) Performance trends of a multi-layer neural network with different numbers of hidden layers but the same total number of nodes (400), evaluated on the spiral benchmark and MNIST datasets.

perform 2- and 3-hidden-layer networks with 1024 nodes (see Fig. 5a), highlighting the importance of networks depth when handling complex nonlinear tasks.

4 Conclusion

Our results suggest that while the performance of fiber-optical ELMs stalls on the MNIST dataset, they excel in handling highly nonlinear tasks. This highlights their suitability for specialized applications where conventional optical neural networks, which are often shallow (i.e., single-layer), face limitations.

To date, the performance gain in optical neural networks is traditionally shown in improvements in image classification results across various datasets, including MNIST, fashion-MNIST, ImageNet. While these datasets are widely used, they fail to isolate the performance gains

achieved through nonlinearity from those resulting from increased network connectivity. We demonstrated that measuring the system’s nonlinear inference capacity through scalable nonlinear benchmarks, such as the spiral dataset, provides a less ambiguous way to compare the computational depth of unconventional neuromorphic hardware. The spiral benchmark’s key strength lies in its parametric nature, allowing controlled increases in task complexity that directly test a system’s nonlinear inference capacity. This approach has proven especially valuable in two critical aspects: First, it enables quantitative comparison between different analog computing substrates, whose computational operations are often difficult to enumerate in the number of performed computes. Second, it establishes a direct bridge between physical implementations and digital models, allowing us to correlate the scaling of physical system dynamics with the depth of digital neural networks. These findings may pave the way for a framework for developing standardized benchmarks that can effectively evaluate both conventional and physics-inspired computing architectures, particularly in their ability to handle increasingly complex nonlinear tasks.

We furthermore observe a direct separation of the spiral classes in selected output channels of our systems, which uniquely showcase nonlinear Schrödinger systems as genuinely arbitrary kernel machines, providing a unique substrate for implementing the ELM computing framework. The soliton number serves as a valuable, platform-independent measure of the nonlinear inference capacity. By incorporating this parameter, we gain a nuanced understanding of the system’s behavior and its ability to process complex inputs effectively.

Through our work, we hope to encourage ongoing exploration of generalizable performance metrics, as the connection between data-driven inference performance and the measures of intricate physical dynamics may prove vital in uncovering the genuine computational performance of natural systems. Information measures, such as Shannon Entropy [33], Fischer Information [34], or Information Processing Capacity [35] may provide a profound start, yet their application to analog feedforward ELMs remains unclear.

Our findings collectively highlight the promise of the fiber-optical Schrödinger system as a scalable, efficient solution for neuromorphic computing. Their capability to handle highly nonlinear tasks with a compact and stable design positions them as a strong candidate for advancing future computing systems, in particular in a more open approach to unconventional neuromorphic computing frameworks that go beyond the perceptron architecture.

Acknowledgements: We acknowledge that this work was made possible by funding from the Carl Zeiss Foundation through the NEXUS program (project P2021-05-025).

Research Funding: Carl Zeiss Stiftung

Author Contributions: S.S. did the data acquisition, data analysis, modeling, and coding, and contributed to writing, proof reading, figure editing, and methods development. M.C. led the project, supervised the data acquisition,

data analysis, modeling, and coding, and contributed to writing, proof reading, figure editing, and methods development. M.C. and B.F. designed the setup. B.F. also contributed to optimizing the experiments, coding, proof reading, methods development and figure editing. M.M. contributed to optimizing the experiments, coding, proof reading. G.R.C. contributed to data analysis, coding, and proof reading. T.B. contributed to modeling and proof reading.

Conflict of Interest Statement: The authors declare no conflict of interest regarding the publication of this paper.

Data Availability: The used raw spiral benchmark data is available on our Github page. DOI: 10.5281/zenodo.14773759.

References

- [1] Sudip Shekhar, Wim Bogaerts, Lukas Chrostowski, John E. Bowers, Michael Hochberg, Richard Soref, and Bhavin J. Shastri. Roadmapping the next generation of silicon photonics. 15(1):751. ISSN 2041-1723. doi:10.1038/s41467-024-44750-0. URL <https://www.nature.com/articles/s41467-024-44750-0>. Publisher: Nature Publishing Group.
- [2] Bhavin J. Shastri, Alexander N. Tait, Mitchell A. Nahmias, Ben Wu, and Paul R. Prucnal. Spatiotemporal pattern recognition with cascaded graphene excitable lasers. In *2014 IEEE Photonics Conference*, pages 573–574. IEEE. ISBN 978-1-4577-1504-4. doi:10.1109/IPCon.2014.6995270. URL <http://ieeexplore.ieee.org/document/6995270/>.
- [3] Saumil Bandyopadhyay, Alexander Sludds, Stefan Krastanov, Ryan Hamerly, Nicholas Harris, Darius Bunandar, Matthew Streshinsky, Michael Hochberg, and Dirk Englund. Single-chip photonic deep neural network with forward-only training. 18(12):1335–1343. ISSN 1749-4885, 1749-4893. doi:10.1038/s41566-024-01567-z. URL <https://www.nature.com/articles/s41566-024-01567-z>.
- [4] Oceane Destras, Sébastien Le Beux, Felipe Gohring De Magalhães, and Gabriela Nicolescu. Survey on activation functions for optical neural networks. 56(2):1–30. ISSN 0360-0300, 1557-7341. doi:10.1145/3607533. URL <https://dl.acm.org/doi/10.1145/3607533>.
- [5] Danijela Marković, Alice Mizrahi, Damien Querlioz, and Julie Grollier. Physics for neuromorphic computing. 2(9):499–510. ISSN 2522-5820. doi:10.1038/s42254-020-0208-2. URL <https://doi.org/10.1038/s42254-020-0208-2>.
- [6] S. Ortín, M. C. Soriano, L. Pesquera, D. Brunner, D. San-Martín, I. Fischer, C. R. Mirasso, and J. M. Gutiérrez. A unified framework for reservoir computing and extreme learning machines based on a single time-delayed neuron. 5(1):14945. ISSN 2045-2322. doi:10.1038/srep14945. URL <http://www.nature.com/articles/srep14945>.
- [7] François Duport, Bendix Schneider, Anteo Smerieri, Marc Haelterman, and Serge Massar. All-optical reservoir computing. *Opt. Express*, 20(20):22783–22795, Sep 2012. doi:10.1364/OE.20.022783. URL <https://opg.optica.org/oe/abstract.cfm?URI=oe-20-20-22783>.
- [8] Kalpak Gupta, Ye-Ryoung Lee, Ye-Chan Cho, and Wonshik Choi. Multilayer optical neural network using saturable absorber for nonlinearity. 577:131471. ISSN 00304018. doi:10.1016/j.optcom.2024.131471. URL <https://linkinghub.elsevier.com/retrieve/pii/S0030401824012082>.
- [9] Anas Skalli, Joshua Robertson, Dafydd Owen-News, Matej Hejda, Xavier Porte, Stephan Reitzenstein, Antonio Hurtado, and Daniel Brunner. Photonic neuromorphic computing using vertical cavity semiconductor lasers. 12(6):2395. ISSN 2159-3930. doi:10.1364/OME.450926. URL <https://opg.optica.org/abstract.cfm?URI=ome-12-6-2395>.
- [10] Clara C. Wanjura and Florian Marquardt. Fully nonlinear neuromorphic computing with linear wave scattering. 20(9):1434–1440. ISSN 1745-2481. doi:10.1038/s41567-024-02534-9. URL <https://www.nature.com/articles/s41567-024-02534-9>. Publisher: Nature Publishing Group.
- [11] Fei Xia, Kyungduk Kim, Yaniv Eliezer, SeungYun Han, Liam Shaughnessy, Sylvain Gigan, and Hui Cao. Nonlinear optical encoding enabled by recurrent linear scattering. pages 1–9. ISSN 1749-4893. doi:10.1038/s41566-024-01493-0. URL <https://www.nature.com/articles/s41566-024-01493-0>.
- [12] Gouhei Tanaka, Toshiyuki Yamane, Jean Benoit Héroux, Ryosho Nakane, Naoki Kanazawa, Seiji Takeda, Hidetoshi Numata, Daiju Nakano, and Akira Hirose. Recent advances in physical reservoir computing: A review. 115:100–123. ISSN 0893-6080. doi:10.1016/j.neunet.2019.03.005. URL <https://www.sciencedirect.com/science/article/pii/S0893608019300784>.
- [13] Guy Van Der Sande, Daniel Brunner, and Miguel C. Soriano. Advances in photonic reservoir computing. 6(3):561–576. ISSN 2192-8614, 2192-8606. doi:10.1515/nanoph-2016-0132. URL <https://www.degruyter.com/document/doi/10.1515/nanoph-2016-0132/html>.
- [14] Giulia Marcucci, Davide Pierangeli, and Claudio Conti. Theory of neuromorphic computing by waves: Machine learning by rogue waves, dispersive shocks, and solitons. 125(9):093901. ISSN 0031-9007, 1079-7114. doi:10.1103/PhysRevLett.125.093901.

- URL <https://link.aps.org/doi/10.1103/PhysRevLett.125.093901>.
- [15] Uğur Teğın, Mustafa Yıldırım, İlker Oğuz, Christophe Moser, and Demetri Psaltis. Scalable optical learning operator. 1(8):542–549. ISSN 2662-8457. doi:10.1038/s43588-021-00112-0. URL <https://www.nature.com/articles/s43588-021-00112-0>.
- [16] Tingyi Zhou, Fabien Scalzo, and Bahram Jalali. Nonlinear schrödinger kernel for hardware acceleration of machine learning. 40(5):1308–1319. ISSN 0733-8724. doi:10.1109/JLT.2022.3146131. URL <https://ieeexplore.ieee.org/document/9695395/>.
- [17] Bennet Fischer, Mario Chemnitz, Yi Zhu, Nicolas Perron, Piotr Roztockı, Benjamin MacLellan, Luigi Di Lauro, A. Aadhi, Cristina Rimoldi, Tiago H. Falk, and Roberto Morandotti. Neuromorphic computing via fission-based broadband frequency generation. 10(35):2303835. ISSN 2198-3844, 2198-3844. doi:10.1002/advs.202303835. URL <https://onlinelibrary.wiley.com/doi/10.1002/advs.202303835>.
- [18] Marina Zajnulina, Alessandro Lupo, and Serge Massar. Weak kerr nonlinearity boosts the performance of frequency-multiplexed photonic extreme learning machines: A multifaceted approach. URL <http://arxiv.org/abs/2312.12296>.
- [19] Akmaljon Palvanov and Young Im Cho. Comparisons of deep learning algorithms for MNIST in real-time environment. 18(2):126–134. ISSN 1598-2645, 2093-744X. doi:10.5391/IJFIS.2018.18.2.126. URL http://www.ijfis.org/journal/view.html?uid=824&sort=&scale=&key=year&keyword=&s_v=18&s_n=2&pn=vol&year=2018&vmd=Full.
- [20] Guang-Bin Huang, Qin-Yu Zhu, and Chee-Kheong Siew. Extreme learning machine: Theory and applications. 70(1):489–501. ISSN 09252312. doi:10.1016/j.neucom.2005.12.126. URL <https://linkinghub.elsevier.com/retrieve/pii/S0925231206000385>.
- [21] Xinchun Gao, Yawei Li, Wen Li, Lixin Duan, Luc Van Gool, Luca Benini, and Michele Magno. Learning continuous piecewise non-linear activation functions for deep neural networks. In *2023 IEEE International Conference on Multimedia and Expo (ICME)*, pages 1835–1840. doi:10.1109/ICME55011.2023.00315. URL <https://ieeexplore.ieee.org/document/10219752>. ISSN: 1945-788X.
- [22] Anatoly Efimov, Mark D. Moores, Nicole M. Beach, Jeffrey L. Krause, and David H. Reitze. Adaptive control of pulse phase in a chirped-pulse amplifier. *Opt. Lett.*, 23(24):1915–1917, Dec 1998. doi:10.1364/OL.23.001915. URL <https://opg.optica.org/ol/abstract.cfm?URI=ol-23-24-1915>.
- [23] Bennet Fischer, Mehmet Müftüoğlu, and Mario Chemnitz. Machine-aided near-transform-limited pulse compression in fully fiber-interconnected systems for efficient spectral broadening. In John M. Dudley, Anna C. Peacock, Birgit Stiller, and Giovanna Tissoni, editors, *Nonlinear Optics and its Applications 2024*, volume 13004, page 1300402. International Society for Optics and Photonics, SPIE, 2024. doi:10.1117/12.3022291. URL <https://doi.org/10.1117/12.3022291>.
- [24] L. Appeltant, M.C. Soriano, G. Van Der Sande, J. Danckaert, S. Massar, J. Dambre, B. Schrauwen, C.R. Mirasso, and I. Fischer. Information processing using a single dynamical node as complex system. *Nature Communications*, 2(1):468, September 2011. ISSN 2041-1723. doi:10.1038/ncomms1476. URL <https://www.nature.com/articles/ncomms1476>.
- [25] L. Larger, M. C. Soriano, D. Brunner, L. Appeltant, J. M. Gutierrez, L. Pesquera, C. R. Mirasso, and I. Fischer. Photonic information processing beyond turing: an optoelectronic implementation of reservoir computing. 20(3):3241. ISSN 1094-4087. doi:10.1364/OE.20.003241. URL <https://opg.optica.org/oe/abstract.cfm?uri=oe-20-3-3241>.
- [26] Y. Paquot, F. Duport, A. Smerieri, J. Dambre, B. Schrauwen, M. Haelterman, and S. Massar. Optoelectronic reservoir computing. 2(1):287. ISSN 2045-2322. doi:10.1038/srep00287. URL <https://www.nature.com/articles/srep00287>.
- [27] Romain Martinenghi, Sergei Rybalko, Maxime Jacquot, Yanne K. Chembo, and Laurent Larger. Photonic nonlinear transient computing with multiple-delay wavelength dynamics. 108(24):244101. ISSN 0031-9007, 1079-7114. doi:10.1103/PhysRevLett.108.244101. URL <https://link.aps.org/doi/10.1103/PhysRevLett.108.244101>.
- [28] Hong Chang and Dit-Yan Yeung. Robust path-based spectral clustering. 41(1):191–203. ISSN 00313203. doi:10.1016/j.patcog.2007.04.010. URL <https://linkinghub.elsevier.com/retrieve/pii/S0031320307002038>.
- [29] H. Zhang, M. Gu, X. D. Jiang, J. Thompson, H. Cai, S. Paesani, R. Santagati, A. Laing, Y. Zhang, M. H. Yung, Y. Z. Shi, F. K. Muhammad, G. Q. Lo, X. S. Luo, B. Dong, D. L. Kwong, L. C. Kwek, and A. Q. Liu. An optical neural chip for implementing complex-valued neural network. 12(1):457. ISSN 2041-1723. doi:10.1038/s41467-020-20719-7. URL <https://www.nature.com/articles/s41467-020-20719-7>.
- [30] Alexander Song, Sai Nikhilesh Murty Kottapalli, Rahul Goyal, Bernhard Schölkopf, and Peer Fischer. Low-power scalable multilayer optoelectronic neural networks enabled with incoherent light. 15(1):10692.

ISSN 2041-1723. doi:10.1038/s41467-024-55139-4. URL <https://www.nature.com/articles/s41467-024-55139-4>.

- [31] Mathilde Hary, Daniel Brunner, Lev Leybov, Piotr Ryczkowski, John M. Dudley, and Goëry Genty. Principles and metrics of extreme learning machines using a highly nonlinear fiber. URL <http://arxiv.org/abs/2501.05233>.
- [32] David Castelló-Lurbe, Antonio Carrascosa, Enrique Silvestre, Antonio Díez, Jürgen Van Erps, Nathalie Vermeulen, and Miguel V. Andrés. Measurement of the soliton number in guiding media through continuum generation. *Opt. Lett.*, 45(16): 4432–4435, Aug 2020. doi:10.1364/OL.399382. URL <https://opg.optica.org/ol/abstract.cfm?URI=ol-45-16-4432>.
- [33] Marina Zajnulina. Shannon entropy helps optimize the performance of a frequency-multiplexed extreme learning machine. URL <http://arxiv.org/abs/2408.07108>.
- [34] Stefan Rotter. The concept of fisher information in scattering problems and neural networks. In *Nonlinear Optics and its Applications 2024*, volume PC13004, page PC1300401. SPIE. doi:10.1117/12.3022535.
- [35] Joni Dambre, David Verstraeten, Benjamin Schrauwen, and Serge Massar. Information processing capacity of dynamical systems. *Scientific Reports*, 2:514, 2012. doi:10.1038/srep00514.

5 Appendix

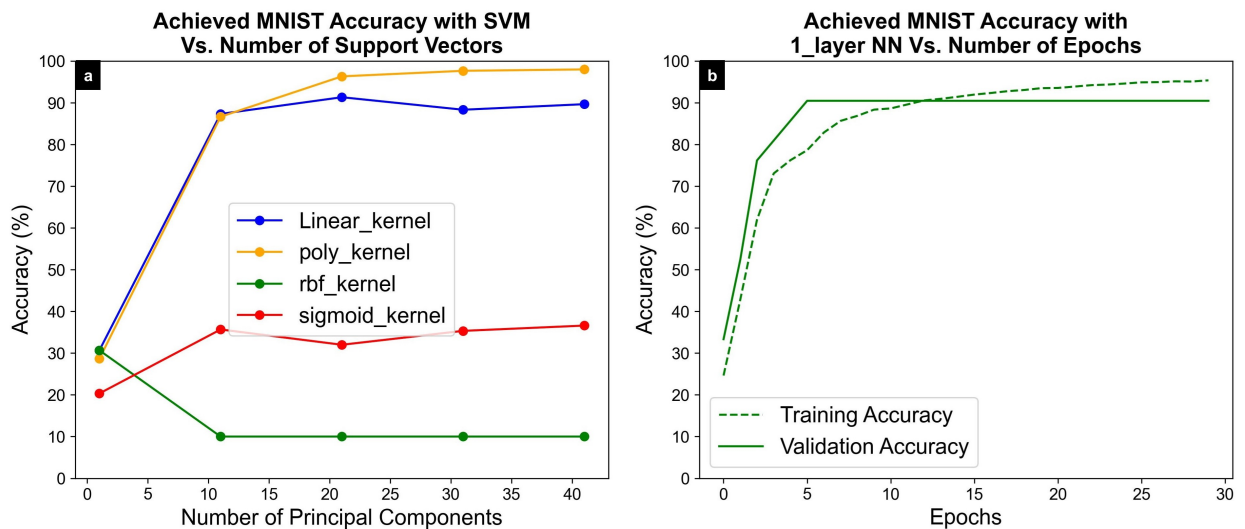


Figure 1A: (a) Test accuracy achieved on the MNIST dataset using Support Vector Machines (SVM) with different kernels, plotted against the number of support vectors used. (b) Test accuracy achieved on the MNIST dataset using a one-layer MLP with 10 hidden nodes, evaluated across different numbers of training epochs.

Table 1A: First MLP, distribution of nodes (1024) across hidden layers, corresponds to the results shown in figure 6

Hidden layers	First layer	Second layer	Third layer	Fourth layer	Fifth layer
1	1024				
2	512	512			
3	512	256	256		
4	512	256	128	128	
5	512	256	128	64	64

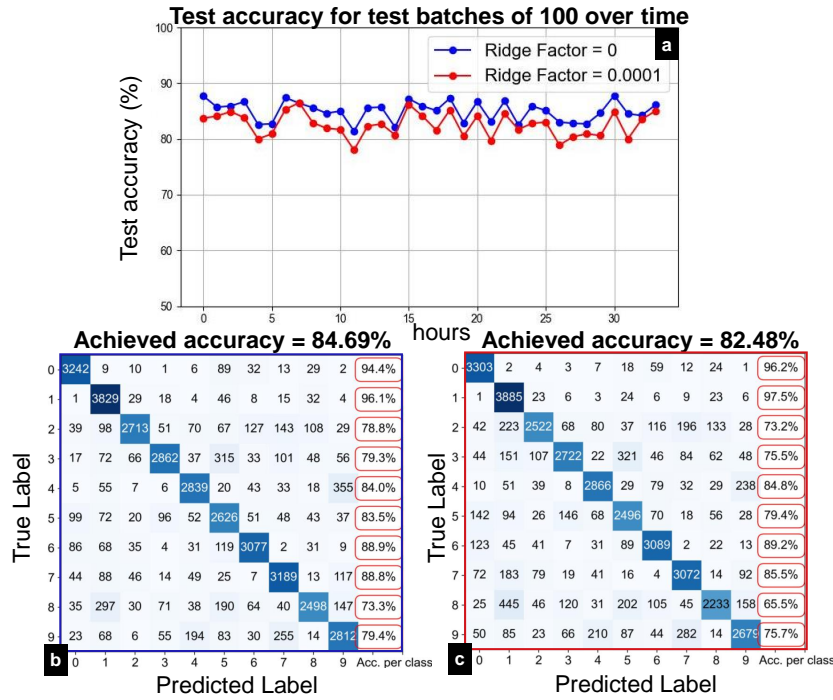


Figure 2A: (a) Test accuracy achieved on MNIST samples recorded over a 35-hour period. Each test sample consists of 1000 images, while 3000 images were used for training the system, we trained the system and with and without applying a ridge factor. (b-C) Test-data confusion matrices for both cases.

Table 2A: Second MLP, distribution of nodes (400) across hidden layers, corresponds to the results shown in figure 6

Hidden layers	First layer	Second layer	Third layer	Fourth layer	Fifth layer
1	400				
2	200	200			
3	200	100	100		
4	200	100	50	50	
5	125	100	75	50	50

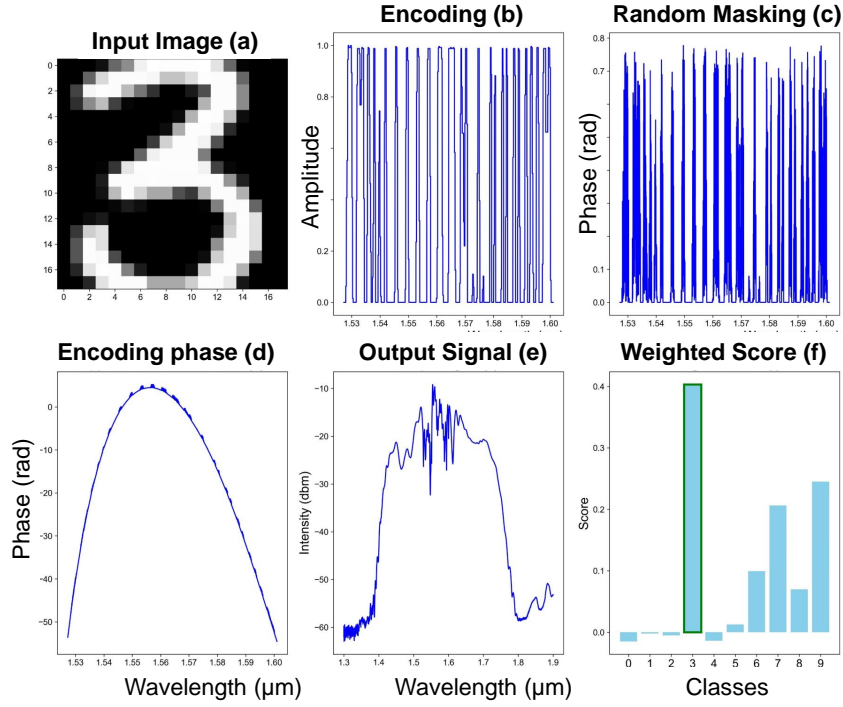


Figure 3A: (a) Input MNIST image cropped to an 18×18-pixel window. (b) The corresponding 1D signal derived from flattening the input image. (c) The resulting encoded signal after multiplying the 1D signal by a random signal and the phase scale factor. (d) Encoding phase, generated by adding the masked signal to the optimized zero-phase profile. (e) The corresponding spectral output signal. (f) The weighted output score, obtained by multiplying the read-outs with the trained weight matrix. A winner-takes-all approach is applied, where the predicted class corresponds to the maximum score; in this case, the predicted class is "3".

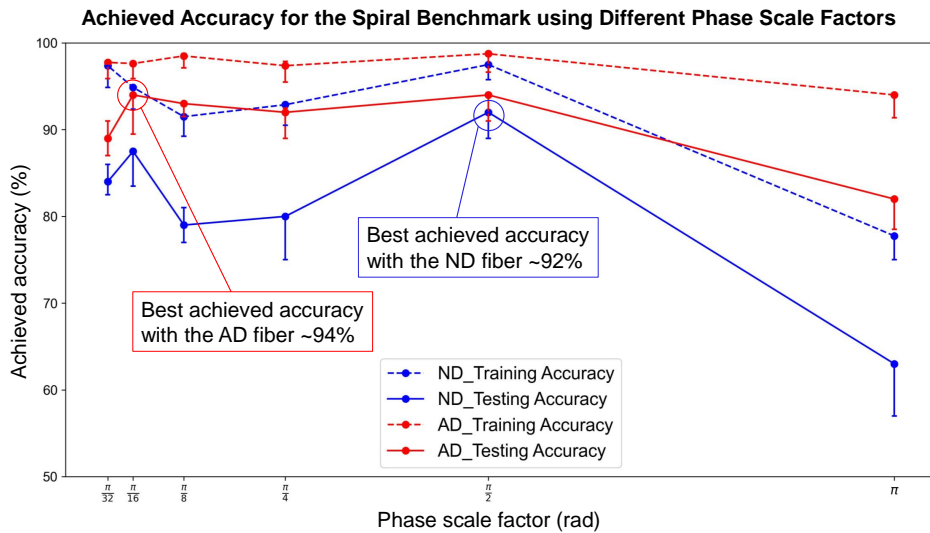


Figure 4A: The achieved accuracy for the spiral benchmark with $\theta_{max} = 10\pi$, evaluated using different phase scale factors. All results were recorded under consistent conditions, including zero attenuation (0 dB) and identical training and testing samples.